

Frustration-Enhanced Quantum Annealing Correction Models with Additional Inter-replica Interactions

Tomohiro Hattori¹

¹ Graduate School of Science and Technology, Keio University,
3-14-1 Hiyoshi, Kohoku-ku, Yokohama-shi, Kanagawa 223-8522, Japan

Shu Tanaka^{1,2,3,4}

² Department of Applied Physics and Physico-Informatics, Keio University,
3-14-1 Hiyoshi, Kohoku-ku, Yokohama-shi, Kanagawa 223-8522, Japan

³ Keio University Sustainable Quantum Artificial Intelligence Center (KSQAIC), Keio University, Tokyo 108-8345, Japan

⁴ Human Biology-Microbiome-Quantum Research Center (WPI-Bio2Q), Keio University, Tokyo 108-8345, Japan
(Dated: September 16, 2025)

Quantum annealing correction (QAC) models provide a promising approach for mitigating errors in quantum annealers. Previous studies have established that QAC models are crucial for ensuring the robustness of the ground state of the Ising model on hardware. In this work, the effects of QAC models incorporating replicas with additional interactions, specifically, the *penalty spin model* and the *stacked model*, are investigated for problems characterized by a small energy gap between the ground and first excited states during quantum annealing, a well-known bottleneck to reaching the ground state. The results demonstrate that these QAC models can obtain the optimal solution within short annealing times by exploiting diabatic transitions, even for problems with a small energy gap. These findings highlight the potential of QAC models as practical near-term algorithms for hardware subject to runtime limitations and control noise.

Keywords: Combinatorial optimization, Quantum annealing, Quantum annealing correction, Penalty spin model, Stacked model, Frustration, Diabatic quantum annealing

I. INTRODUCTION

Quantum Annealing (QA) [1–6] has the potential to solve combinatorial optimization problems with both high accuracy and efficiency. Recently, various QA-based algorithms have been developed for practical use, including size reduction methods [7–13], quantum-classical hybrid methods [14–16], and error mitigation methods [17, 18]. Moreover, QA and QA-inspired methods have been applied to diverse domains, including advertisement optimization [19], black-box optimization [20–26], computer-aided engineering [27–31], and finance [32, 33].

The adiabatic theorem [34] guarantees that the ground state of the Ising model, which corresponds to the optimal solution of the combinatorial optimization problems [35], is obtained at the final time of QA with sufficiently long annealing time. Previous studies [3–6, 34] have discussed the adiabatic condition, which determines the required annealing time to obtain the ground state of the Ising model. The adiabatic condition guarantees instantaneously following the ground state of the system during QA with an annealing time that scales with the inverse square of the minimum energy gap between the ground state and the first excited state. However, bottlenecks such as a small energy gap [36], hardware control noise [37], and decoherence [38] hinder the achievement of high-quality solutions. Therefore, algorithms are needed to overcome these bottlenecks.

Expanding the energy gap is one promising approach. Previous studies have demonstrated improvements in the scaling of the energy gap, both analytically and numerically [36, 39–47]. Although numerous methods have

achieved exponential improvements in energy-gap scaling, significant difficulties remain in their practical implementation on quantum hardware and in their limited applicability under specific enhancement conditions.

Exploiting diabatic transitions during QA is another promising approach for overcoming the small energy gap [16, 48–50]. Diabatic QA, which allows the diabatic transition during QA, has been shown to benefit both combinatorial optimization and sampling tasks [48]. Moreover, annealing schedule optimization is a promising way to exploit diabatic transition during QA [16, 49]. Although the transferability of annealing schedules reduces the cost of the schedule optimization [16], the applicability remains limited for similar problem instances. These methods exploiting diabatic transitions are important as near-term algorithms, since diabatic transitions are inevitable in current hardware.

The parallel QA has been proposed to effectively use the idle quantum bits (qubits), thereby improving the time-to-solution (TTS) in real quantum annealers [51]. Also, previous studies have proposed the quantum annealing correction (QAC) models to enhance the robustness of the ground state of the Ising model against control errors [37, 52–63], and demonstrated better performance than parallel QA. In the previous studies, errors in a random error Ising model were suppressed [52] by introducing additional interactions between each spin and a *penalty spin*. A penalty spin acts as a slack spin that imposes an energetic penalty when spins across replicas are not aligned. This QAC model is referred to as the *penalty spin model*. Consequently, the additional interactions cause the spins in each replica to align in the same

direction, thereby protecting the quantum state from errors. The penalty spin model is particularly effective when the success probability of each replica is relatively high, as it resembles the majority-vote scheme in coding theory. Analytical studies of penalty spin models have also been actively pursued [57, 59].

The nested quantum annealing correction (NQAC) model [56, 61] is an extension of QAC models that introduces a nested structure to enhance both error resilience and solution quality by adding ferromagnetic interactions that align the replicas in the same direction. This structure mitigates spin flips, chain breaks, and other hardware-induced errors, resulting in stable success probabilities that are largely independent of the number of replicas. The NQAC model has been shown to be effective even for Boltzmann sampling via QA [64, 65]. The effectiveness of antiferromagnetic interactions has been validated in the NQAC model. However, the mechanism underlying this performance improvement remains unclear.

Another promising QAC approach is the stacked model, which utilizes replicas of the Ising model on hardware and incorporates additional interactions between replicas [62, 63, 66]. Previous studies demonstrated the robustness of the ground state of the Ising model for both the Sherrington–Kirkpatrick model and the antiferromagnetic chain [62, 63]. Additionally, they investigated in detail how and when antiferromagnetic interactions between replicas can effectively reduce bit-flip errors, and they estimated the extent of error reduction achieved. However, the dynamics of QA and the performance on actual quantum annealers have not been studied in instances with a small energy gap between the ground state and the first excited state. Adding slack spins may hinder the solution quality by increasing the number of spins, as suggested in the previous studies [11, 12]. Therefore, it is crucial to investigate the properties of the QAC models and whether they hinder the performance.

In this study, we examined QAC models applied to problems characterized by a small energy gap during QA. In QAC models, the optimal solution may appear in certain excited eigenstates after decoding, thus, even if the quantum state does not reach the ground state, the optimal solution can still be obtained. Therefore, under conditions where the state is easily excited due to the small energy gap, decoherence, or control noise, QAC models can still yield the optimal solution. To evaluate the effects of the QAC models, we used the frustrated ring model as a benchmark problem, since it exhibits spin-glass bottlenecks on quantum annealers [67].

The remainder of this paper is organized as follows. Section II introduces QA and QAC models. Section III describes the frustrated ring model, experimental setup, numerical methods, and evaluation methods. Section IV analyzes the effects of the QAC models in experiments and numerical simulations, focusing on success probability and the properties of the energy spectrum during QA from the perspective of diabatic QA. Finally, Section V

presents our conclusions and outlines future directions.

II. METHOD

In QA, the optimal solution of a combinatorial optimization problem corresponds to the ground state of the Ising model. The Hamiltonian of the QA is expressed as follows:

$$\mathcal{H}(t) = A(t)\mathcal{H}_q + B(t)\mathcal{H}_p, \quad 0 \leq t \leq \tau, \quad (1)$$

where τ is the annealing time, \mathcal{H}_q is the driver Hamiltonian, \mathcal{H}_p is the problem Hamiltonian, and $A(t)$ and $B(t)$ are real-valued functions called annealing schedules. The annealing schedules satisfy $A(0) \gg B(0)$ and $A(\tau) \ll B(\tau)$. Many combinatorial optimization problems can be formulated as an Ising model by corresponding their optimal solution of the combinatorial optimization problems and the ground state of the Ising model [35]. In QA, the problem Hamiltonian is represented by the Ising model. A transverse field is generally used as the driver Hamiltonian. QA ideally aims for the quantum state to follow the instantaneous ground state of the system. Therefore, the initial state is the ground state of \mathcal{H}_q .

The transverse-field and problem Hamiltonians are respectively expressed as follows:

$$\mathcal{H}_q = - \sum_{i=1}^N \sigma_i^x, \quad (2)$$

$$\mathcal{H}_p = - \sum_{i=1}^N h_i \sigma_i^z - \sum_{1 \leq i < j \leq N} J_{i,j} \sigma_i^z \sigma_j^z, \quad (3)$$

where σ_i^α ($\alpha = x, y, z$) is the α -component of the Pauli operator on vertex i and N is the number of spins. Here, h_i and $J_{i,j}$ are the longitudinal magnetic fields at spin i and the interactions between spin i and j , respectively. The initial state is the equal superposition state of all computational basis states, which corresponds to the ground state of \mathcal{H}_q . The formulation of \mathcal{H}_p in Eq. (3) is the standard form used in QA, which we call the *unprotected model* as shown in Fig. 1 (a).

The required number of spins is $N \times K$ in the QAC models. The unpenalized parallel Ising model, referred to as the *classical model* [52, 53], was also proposed as a form of parallel QA in a previous study [51]. A schematic diagram of the classical model is shown in Fig. 1 (b). We define the Hamiltonian of the k th replica of the QAC model as

$$\mathcal{H}_p^{(k)} = - \sum_{i=1}^N h_i \sigma_{i,k}^z - \sum_{1 \leq i < j \leq N} J_{i,j} \sigma_{i,k}^z \sigma_{j,k}^z. \quad (4)$$

Here, $\sigma_{i,k}^\alpha$ ($\alpha = x, y, z$) denotes the α -component of the Pauli matrix on vertex i in the k th replica. In the classi-

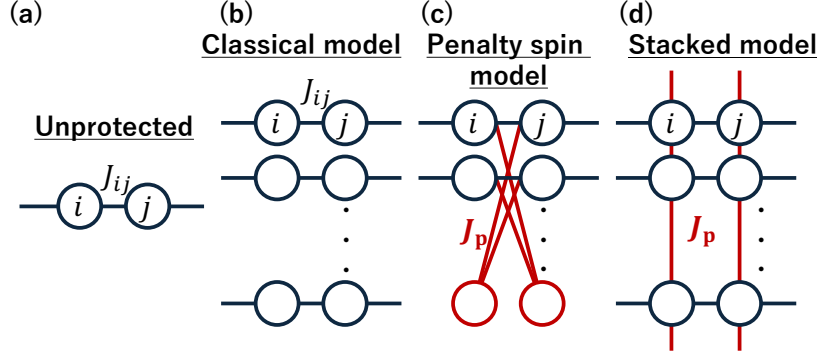


FIG. 1. Schematic diagrams of the QAC models: (a) the unprotected model, (b) the classical model, (c) the penalty spin model, (d) the stacked model. The penalty spin model and the stacked model use replicas with additional interactions. The circles represent the spins, and the solid lines represent the interactions. The red circles represent the slack spins, and the red solid lines represent the additional interactions.

cal model, the Hamiltonian is given by

$$\mathcal{H}_C = \sum_{k=1}^K \mathcal{H}_p^{(k)}, \quad (5)$$

where K denotes the number of replicas.

The *penalty spin model* has been proposed as a QAC model that employs replicas and additional interactions [37, 52–54, 56]. A schematic diagram of the penalty spin model is shown in Fig. 1 (c). The penalty spin model protects the quantum states from errors such as decoherence and bond chaos. In the penalty spin model, the additional interactions between each spin and the *penalty spin* are introduced. A penalty spin acts as a slack spin that imposes an energetic penalty when the spins across replicas are not aligned. The formulation of the penalty spin model is as follows:

$$\mathcal{H}_{ps} = \sum_{k=1}^{K-1} \mathcal{H}_p^{(k)} - J_p \sum_{i=1}^N \sum_{k=1}^{K-1} \sigma_{i,k}^z \sigma_{i,K}^z, \quad (6)$$

where $\mathcal{H}_p^{(k)}$ is the same as Eq. (4), and J_p is the interaction strength between each spin and the penalty spin. As shown in Eq. (6), the penalty spin model requires $N \times K$ spins, consisting of $K - 1$ replicas together with N penalty spins. We selected the replica with the lowest energy among all the replicas as a result of the QA with the penalty spin model. In the penalty spin model, spins within each replica effectively align in the same direction regardless of the sign of J_p , while the alignment of the penalty spins depends on the sign of J_p .

In this study, we consider the stacked model as a QAC model, which spatially parallelizes replicas of \mathcal{H}_p with additional inter-replica interactions, as proposed in the previous study [62, 63, 66]. A schematic diagram of the stacked model is shown in Fig. 1 (d). We investigate two boundary conditions in this model: open and periodic. The Hamiltonian of the stacked model with open bound-

ary conditions is given by

$$\mathcal{H}_{\text{stacked}}^{(\text{obc})} = \sum_{k=1}^K \mathcal{H}_p^{(k)} - J_p \sum_{i=1}^N \sum_{k=1}^{K-1} \sigma_{i,k}^z \sigma_{i,k+1}^z, \quad (7)$$

where $\mathcal{H}_p^{(k)}$ is the same as Eq. (4), J_p is the interaction strength between replicas. The Hamiltonian of the stacked model with periodic boundary conditions is given by

$$\mathcal{H}_{\text{stacked}}^{(\text{pbc})} = \sum_{k=1}^K \mathcal{H}_p^{(k)} - J_p \sum_{i=1}^N \sum_{k=1}^K \sigma_{i,k}^z \sigma_{i,k+1}^z. \quad (8)$$

Here, $\sigma_{i,K+1} = \sigma_{i,1}$ for arbitrary i due to the periodic boundary condition. For $J_p > 0$ (ferromagnetic interactions), the additional interactions align spins among different replicas in the same direction. In contrast, the additional interactions with $J_p < 0$ (antiferromagnetic interactions) align spins of nearest-neighbor replicas in opposite directions.

When we apply the QAC models, we replace \mathcal{H}_p shown in Eq. (1) to \mathcal{H}_{ps} shown in Eq. (6) or $\mathcal{H}_{\text{stacked}}^{(\text{obc})}$, $\mathcal{H}_{\text{stacked}}^{(\text{pbc})}$ shown in Eqs. (7), (8). In these QAC models using K replicas, the transverse fields are expressed as follows:

$$\mathcal{H}_q^{(K)} = - \sum_{k=1}^K \sum_{i=1}^N \sigma_{i,k}^x. \quad (9)$$

Decoding strategies for QAC models have been discussed in previous studies [52, 53, 55]. These previous studies demonstrated that the energy-minimization strategy is more effective than the majority-vote strategy, which determines spin configurations by a majority rule across parallelized replicas. Therefore, we adopt the energy-minimization strategy for decoding QAC models. In this strategy, the energy of each replica is calculated, and the replica with the lowest energy is selected.

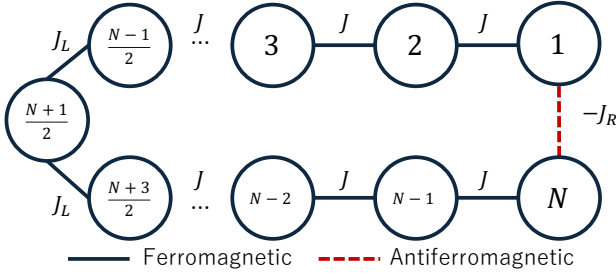


FIG. 2. Schematic diagram of the frustrated ring model with an odd number of spins N . The circles represent the spins, the solid lines represent the ferromagnetic interactions, and the red dashed line represents the antiferromagnetic interaction. The interaction strengths are defined in Eq. (11).

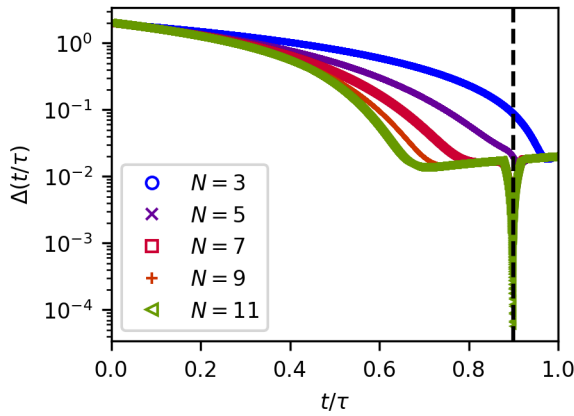


FIG. 3. Energy gap $\Delta(t/\tau)$ between the ground state and the first excited state during QA for the frustrated ring model after removing the degeneracies by adding longitudinal magnetic fields $h_1 = 0.01$. The interactions of the frustrated ring model are $J = 1$, $J_L = 0.45$ and $J_R = 0.5$. The black dashed line indicates the time at which the energy gap closes at $N \rightarrow \infty$, obtained analytically from the frustrated ring model shown in Eq. (10).

III. SETTINGS

In this study, we adopted the frustrated ring model as a benchmark problem because its sparsity results in minimal embedding overhead. Figure 2 shows a schematic diagram of the frustrated ring model with an odd number of spins N . The frustrated ring model is a benchmark problem known to exhibit a spin-glass bottleneck during the QA [68].

The spin-glass bottleneck, a well-known limitation in QA, prevents the quantum state from remaining the instantaneous ground state of the total Hamiltonian. Therefore, obtaining the ground state of the frustrated ring model with conventional QA is difficult. The Hamiltonian of the frustrated ring model is expressed as fol-

lows:

$$\mathcal{H}_{\text{fr}} = - \sum_{i=1}^N J_i \sigma_i^z \sigma_{i+1}^z. \quad (10)$$

The interactions are defined as follows:

$$J_i = \begin{cases} -J_R & \text{if } i = N \\ J_L & \text{if } i = \frac{1}{2}(N \pm 1), \\ J & \text{otherwise} \end{cases} \quad (11)$$

where the interactions satisfy $0 < J_R < J_L < J = 1$, N is odd, and the periodic boundary condition is imposed, such that $i = N+1$ corresponds to $i = 1$. Interactions between nearest-neighbor spins are ferromagnetic, and the interaction between spin 1 and spin N is antiferromagnetic, which introduces frustration in the system.

In this study, to eliminate trivial degeneracies, we applied a small longitudinal magnetic field at site 1, setting $h_1 = 0.01$. The frustrated ring model used in this study is therefore expressed as follows:

$$\mathcal{H}_{\text{fr}} = - \sum_{i=1}^N J_i \sigma_i^z \sigma_{i+1}^z - h_1 \sigma_1^z. \quad (12)$$

In this setting, the ground state of the frustrated ring model is the all-up state, and the first excited state of the frustrated ring model is the all-down state, whereas these two states are degenerate without the longitudinal magnetic field. Under this setting, classical metaheuristics using a single-spin flip, such as simulated annealing [69] and gradient descent methods, are easily trapped in local minima due to the large Hamming distance between the ground state and the first excited state.

Following Ref. [67], we set the parameters of the frustrated ring model in the spin-glass bottleneck region to $J_R = 0.45$ and $J_L = 0.5$. Figure 3 shows the energy gap between the ground state and the first excited state during QA for the frustrated ring model with degeneracies removed. As seen in Fig. 3, the small-gap properties persist even after removing the degeneracies. Therefore, the frustrated ring model remains difficult to solve using both classical metaheuristics and QA.

We evaluated the performance of the QAC models on a quantum annealer. We used `Advantage2_system1.6` as the quantum annealer [70]. The quantum annealer consists of 4594 qubits arranged on the Zephyr graph [71]. Since the Zephyr graph is a two-dimensional lattice with open boundary conditions, the stacked model, whose unprotected model is a one-dimensional chain with open boundary conditions, is embeddable without embedding overhead. We set the number of spins in the unprotected model $N = 11, 21, 31, 41, 51, 61$ and the number of replicas to $K = 1, 10, 15, 20, 25, 30, 35$, considering the overhead arising from differences in the boundary conditions between the Zephyr graph and the QAC models. The annealing time was set to $\tau = 1, 20, 100, 1000, 2000 \mu\text{s}$. We examined the dependence of performance on annealing

time, additional interactions in the QAC models, and the number of spins. The quantum annealer was executed with `num_reads` = 100 and minor embedding was employed [72, 73]. All other parameters were set to their default values.

Next, we numerically examined the effectiveness of the QAC models for the frustrated ring model by solving the time-dependent Schrödinger equation using QuTiP [74, 75]. The annealing schedules are set to $A(t) = 1 - t/\tau$ and $B(t) = t/\tau$ for simplicity. We set the number of spins to $N = 3$ to investigate the dependence of the number of replicas in the numerical analysis. The Schrödinger equation is written as follows:

$$i \frac{\partial}{\partial t} |\psi(t)\rangle = \mathcal{H}(t) |\psi(t)\rangle. \quad (13)$$

Here, Planck units are used.

We evaluated the performance of the QAC models by using the success probability. The success probability is expressed as follows:

$$p(\tau) = \langle \psi(\tau) | P_s | \psi(\tau) \rangle, \quad (14)$$

where $|\psi(t)\rangle$ represents the quantum state at a time τ . The projection operator P_s is defined as

$$P_s = \sum_{i \in S_s} |\phi_i\rangle \langle \phi_i|, \quad (15)$$

where $|\phi_i\rangle$ is the i th eigenstate of the problem Hamiltonian in Eq. (3) and S_s is the set of indices of states including the optimal solution after decoding in the QAC model.

We examined the energy spectrum through numerical exact diagonalization. To reveal the properties of the QAC models, we compared the unprotected model, the classical model, and the QAC models with different numbers of replicas and interaction strengths by using these metrics.

IV. RESULT

We evaluated the performance of QAC models, including the stacked models with both periodic and open boundary conditions, as well as the penalty spin model, using an actual quantum annealer and numerical simulation. Section IV A presents the performance of QAC models on the actual quantum annealer, and Section IV B shows the numerical results.

A. Experiment on an actual quantum annealer

We first examined the effect of additional interactions on the success probability. Figure 4 shows the success probability as a function of the annealing time τ and interaction strength J_p for the frustrated ring model after removing degeneracies with $N = 61$ and $K = 35$.

The results in Fig. 4 consistently demonstrate that additional interactions of moderate strength enhance performance compared with the classical model, whereas ferromagnetic interactions degrade it. Adding interactions increases the energy scale of the system, which can hinder exploration under a fixed transverse-field scale. However, Fig. 4 shows that the additional interactions broaden the accessible low-energy states, facilitating exploration, enabling high-quality solutions to be obtained with shorter annealing times. We next examine each model in detail.

In the periodic-boundary stacked model shown in Fig. 4 (a), introducing antiferromagnetic interactions leads to a higher success probability than that of the classical model. This enhancement is observed regardless of the magnitude of the antiferromagnetic interactions. By contrast, ferromagnetic interactions reduce the success probability.

In the open-boundary stacked model shown in Fig. 4 (b), antiferromagnetic interactions also enhance the success probability relative to the classical model. However, for $J_p = -1$ and $J_p = -0.1$ at $\tau = 2000 \mu s$, the success probability decreases. Consequently, strong interaction strengths tend to decrease the success probability. Ferromagnetic interactions consistently degrade the performance. These findings demonstrate that a higher energy scale leads to a deterioration in solution quality. Furthermore, the distinction between Figs. 4 (a) and (b) arises solely from the boundary conditions. This suggests that the boundary conditions influence the mechanism that leads to higher success probabilities.

In the penalty spin model shown in Fig. 4 (c), similar to the open-boundary stacked model, weak antiferromagnetic interactions (e.g., $J_p = -0.01$) improve the success probability, whereas stronger interactions suppress it. The results indicate that, in the penalty spin model, the improvement occurs only within a narrower range than in the stacked models. Ferromagnetic interactions reduce the success probability except at $J_p = 0.01$. In the penalty spin model, the effect of the additional interactions on the replicas is essentially the same, independent of their sign. Consequently, small interaction strengths, such as $J_p = 0.01$ or $J_p = -0.01$, are most effective in the perspective of achieving a high success probability. The distinct behaviors of ferromagnetic and antiferromagnetic interactions arise from differences in penalty-spin alignment during decoding: with antiferromagnetic interactions, penalty spins align opposite to the replicas, whereas with ferromagnetic interactions, they align in the same direction. This alignment difference directly leads to the observed disparity in success probability. The pronounced nature of this effect suggests that, under the present problem setting, penalty spins frequently correspond to the correct solution state after decoding.

These observations can be explained by the mechanism of replica diversification. In the stacked model, antiferromagnetic interactions align spins of different replicas in opposite directions, broadening access to diverse low-

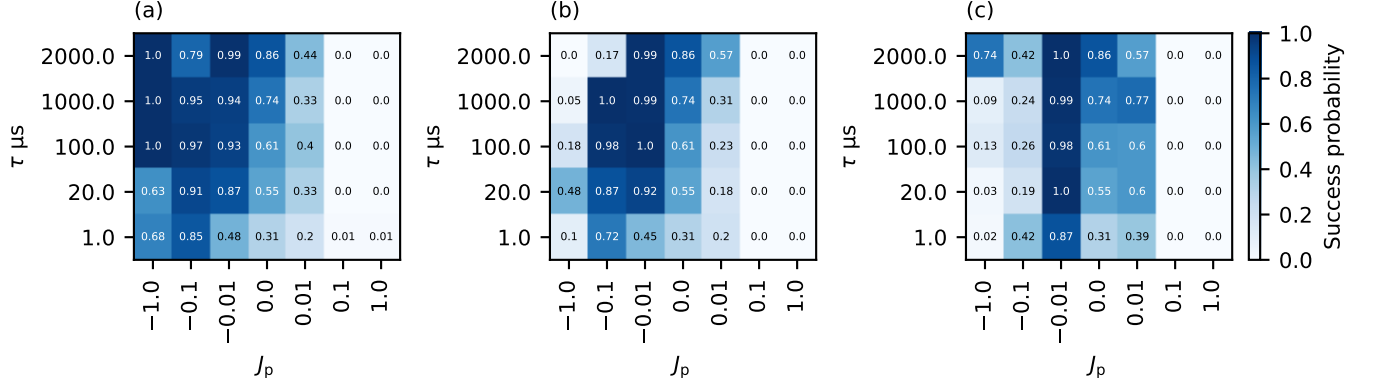


FIG. 4. Final success probability with the different QAC models on an actual quantum annealer as a function of the interaction strength J_p and the annealing time τ μs . The blue bar represents the success probability. The problem size is $N = 61$, with the number of replicas fixed at $K = 35$. Each panel shows the results of (a) the periodic-boundary stacked model, (b) the open-boundary stacked model, and (c) the penalty spin model. The results at $J_p = 0$ correspond to the classical model with $K = 35$.

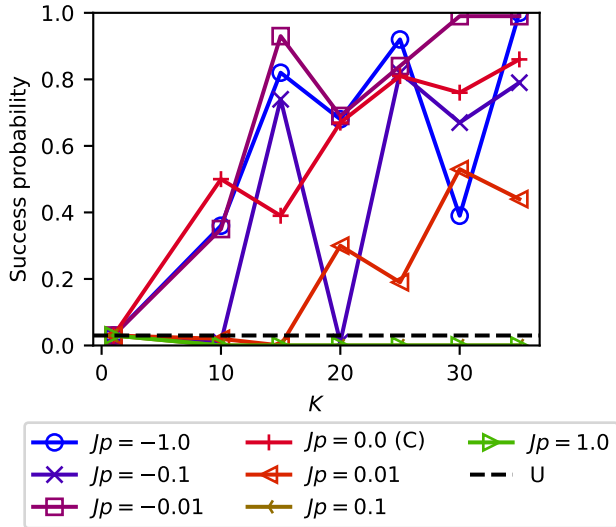


FIG. 5. The final success probability as a function of the number of replicas K with the periodic-boundary stacked model. The problem size is $N = 61$. The annealing time is $\tau = 2000$ μs . The results at $J_p = 0$ correspond to the classical model. The dashed black line represents the success probability of the unprotected model. Solid lines between points are provided as a guide to the eye.

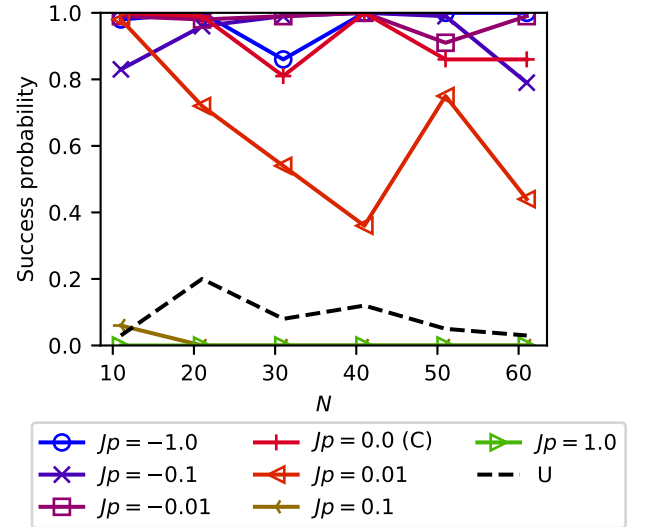


FIG. 6. Scaling of the final success probability of the periodic-boundary stacked model. The number of replicas is fixed to $K = 35$. The annealing time is $\tau = 2000$ μs . The results at $J_p = 0$ correspond to the classical model. The dashed black line represents the result of the success probability with the unprotected model. Solid lines between points are provided as a guide to the eye.

energy states. By contrast, ferromagnetic interactions promote uniform spin alignment across replicas, reducing the diversity of sampled states.

A key factor underlying these behaviors is whether frustration is present among replicas. In the periodic-boundary stacked model, frustration arises only when the number of replicas K is odd, allowing access to a broader set of low-energy states. This explains why high success probabilities persist even for large negative J_p . In all

cases, appropriately tuned antiferromagnetic interactions yield higher success probabilities than the classical model within shorter annealing times. Moreover, the periodic-boundary stacked model requires only minimal tuning, making it easier to apply.

When frustration is absent, the dominant effect of large interaction strengths is the rescaling of the energy spectrum. Previous studies have shown that excessive energy scales degrade solution quality [13, 17]. In

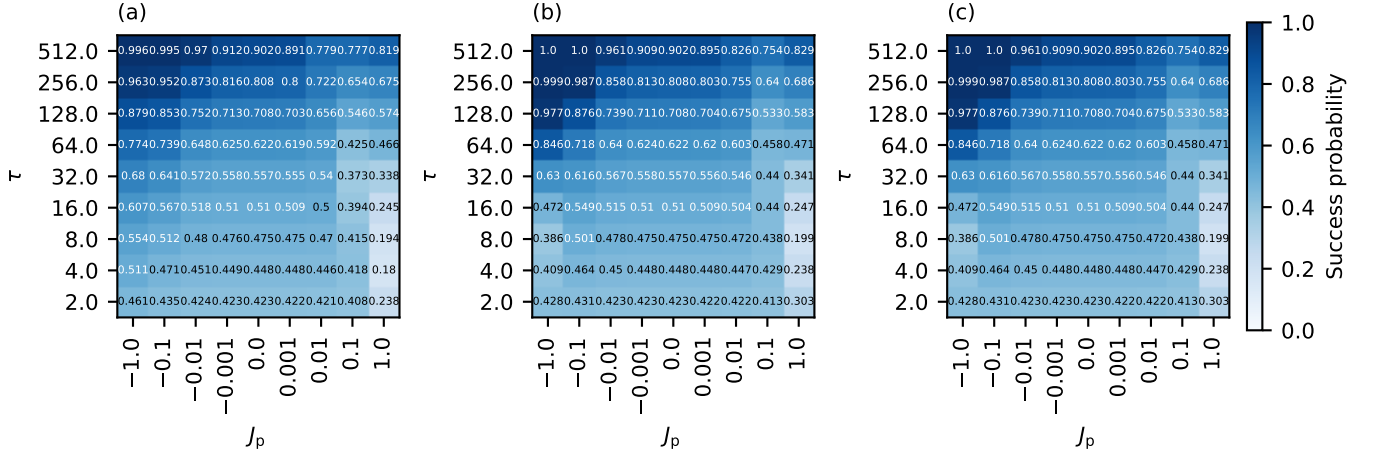


FIG. 7. Final success probability of different QAC models as a function of the interaction strength J_p and the annealing time τ . The blue bars represent the final success probability. The problem size is $N = 3$, with the number of replicas fixed at $K = 3$. Panels show (a) the periodic-boundary stacked model, (b) the open-boundary stacked model, and (c) the penalty spin model. The results at $J_p = 0$ correspond to the classical model with $K = 3$. Results for the classical model are derived from those of the unprotected model.

the open-boundary stacked model and the penalty spin model, where frustration is absent, this rescaling effect governs the performance, resulting in lower success probabilities compared with the periodic-boundary stacked model. The influence of energy scaling is also evident in the annealing-time dependence: larger energy scales require longer annealing times to reliably reach low-energy states. By contrast, in the periodic-boundary stacked model, a high fraction of the diversified low-energy states coincide with the target ground state, enabling robust success probabilities even at short annealing times. We note, however, that stronger interactions in the periodic-boundary stacked model increase the embedding overhead, which may introduce additional errors due to chain breaks; see Appendix A for details.

To further explore the role of frustration, we next examined the periodic-boundary stacked model. Unlike the open-boundary case, the periodic boundary condition introduces replica frustration, which significantly alters the behavior of the system. We examined the dependence of success probability on the number of replicas K .

Figure 5 shows the final success probability as a function of the number of replicas K at $\tau = 2000 \mu\text{s}$ for the frustrated ring model after removing degeneracies with $N = 61$. These results are consistent with those obtained at short annealing times, as shown in Appendix B. With antiferromagnetic interactions of moderate strength, increasing K systematically improves the success probability. However, for $J_p = -1$ and $J_p = -0.1$, the success probability decreases relative to the success probability of the classical model, indicating that fine-tuning of interaction strengths is necessary in that case. By contrast, with ferromagnetic interactions, no such trend is observed. Notably, for large antiferromagnetic interaction strength, the success probability exhibited a strong

even-odd dependence on K , further confirming the importance of frustration in governing performance.

Finally, we analyzed how success probability scales with problem size N . Figure 6 shows the scaling of the final success probability for the frustrated ring model with N after removing degeneracies with $\tau = 2000 \mu\text{s}$ for $K = 35$. As expected, the success probability decreases with increasing N . However, the rate of decrease is significantly mitigated by parallelization: the periodic-boundary stacked model in particular reduces the decay. This trend persists across different system sizes and QAC models, suggesting that the mechanism is robust in QAC models that utilize replicas.

So far, we have presented the results for the frustrated ring model defined in Eq. (12). These observations are consistent with the frustrated ring model defined in Eq. (10). Results and further discussion of success probabilities are provided in Appendix C.

B. Numerical analysis

The numerical simulations are intended not only to reproduce the experimental observations but also to clarify their underlying mechanisms. While the quantum annealer provides success probabilities, the simulations allow analysis of the population distribution and energy spectrum.

Figure 7 shows the success probability as a function of the annealing time τ and interaction strength J_p for the frustrated ring model after removing degeneracies with $N = 3$ and $K = 3$. The simulations also show that antiferromagnetic interactions enhance the success probability, consistent with the experimental observations. This indicates that the advantage of antiferromagnetic inter-

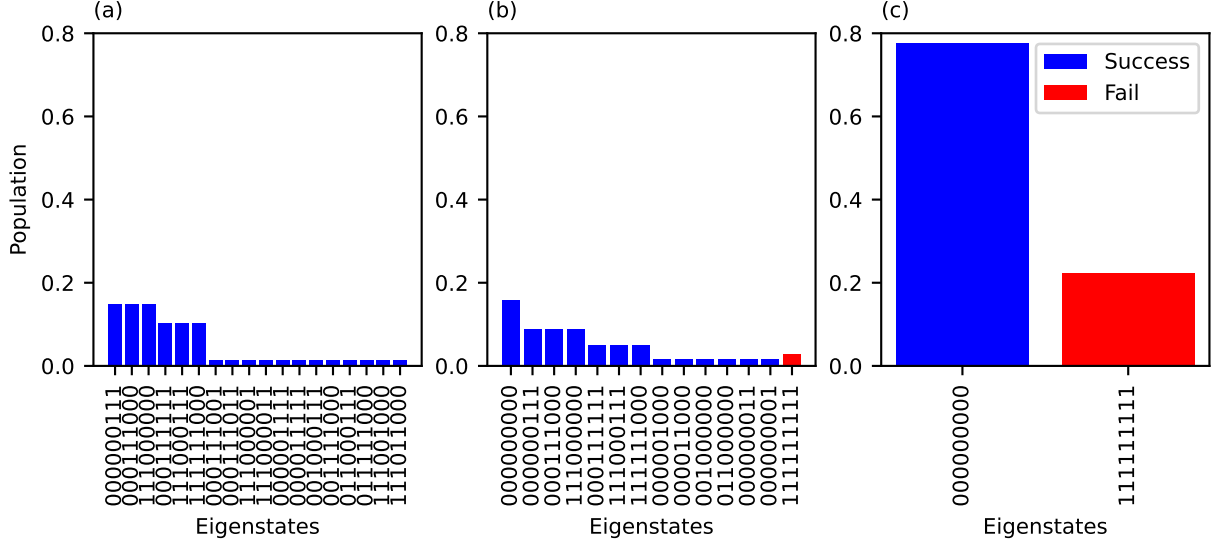


FIG. 8. Final population in the periodic-boundary stacked model. The problem size is $N = 3$, with the number of replicas fixed at $K = 3$. The blue bars represent the success probability. The red bar represents the failure probability. The annealing time is $\tau = 512$. Panels show results for different values of the inter-replica interaction J_p : (a) $J_p = -1$, (b) $J_p = 0$ (classical model) and (c) $J_p = 1$. The eigenstates with probability more than 0.01 are shown. In the bitstring representation, 0 corresponds to the up state ($\sigma_{i,k}^z = +1$), and 1 corresponds to the down state ($\sigma_{i,k}^z = -1$).

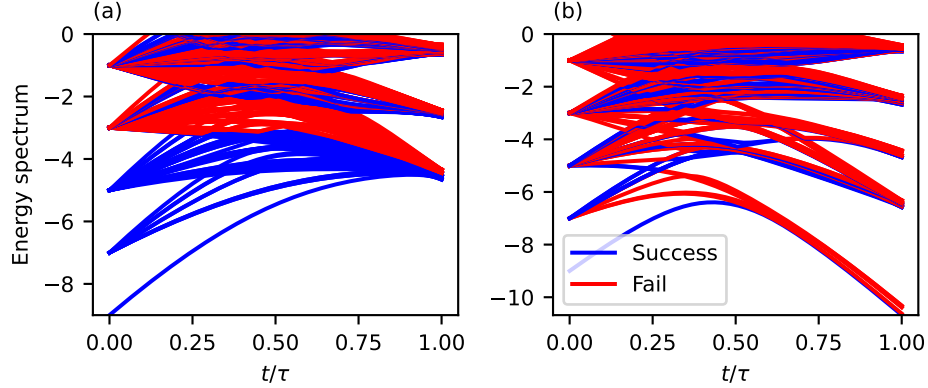


FIG. 9. Energy spectrum during QA for the periodic-boundary stacked model. The problem size is $N = 3$, with the number of replicas fixed at $K = 3$. The blue solid lines represent the energy levels corresponding to the optimal solution after decoding the stacked model, whereas the red solid lines represent those corresponding to the non-optimal solution. Panels show results for different values of the inter-replica interaction J_p : (a) $J_p = -1$, (b) $J_p = 1$.

actions is not merely a hardware-dependent phenomenon but persists in an ideal, noiseless environment.

In the periodic-boundary stacked model shown in Fig. 7 (a), replica frustration enables high success probabilities even at short annealing times, outperforming the classical model. By contrast, in the open-boundary stacked model and the penalty spin model shown in Figs. 7 (b) and (c), the success probability decreases when the annealing time is short and $|J_p|$ is large. These results indicate that energy-scale effects strongly influence success probability and that the replica frustration enhances performance, consistent with the experimental

findings.

We next analyzed the probability distribution of the sampled states, sorted in ascending order of energy, shown in Fig. 8. The results demonstrate that in the periodic-boundary stacked model, success states are broadly distributed among the low-energy states. Consequently, the correct solution can be obtained without requiring fully adiabatic evolution, explaining why this model yields high success probabilities.

By contrast, the classical model has the same energy spectrum as the Hamiltonian of the unprotected model. Therefore, for problem instances intrinsically hard to

solve by QA, parallelization provides little benefit. In theory, the benefit of parallelization scales with the number of replicas K . A detailed discussion is provided in Appendix D. For such hard problems, introducing diversity across replicas is essential for achieving a high success probability.

We also compared the energy spectra obtained by exact diagonalization for different QAC models. Figure 9 shows the energy spectrum of the periodic-boundary stacked model for $J_p = -1$ and $J_p = 1$. In the periodic-boundary stacked model, success states occupy a wide range of low-energy levels, implying that even diabatic time evolution can readily yield correct solutions. The antiferromagnetic interactions preserve the correspondence between the low-energy eigenstates and the optimal solution shown in the previous study [37, 62]. On the other hand, the eigenstates corresponding to the optimal solution spread into higher-energy eigenstates in the periodic-boundary stacked model with ferromagnetic interactions.

In the periodic-boundary stacked model, the decodability of low-energy states varies with different interaction strengths. For $J_p = -1.0$ and -0.1 , the 47 lowest-energy states correspond to the optimal solution. For $J_p = -0.01$, the 38 lowest-energy states correspond to the optimal solution. For $J_p = -0.001, 0, 0.001$, the 6 lowest-energy states correspond to the optimal solution. For $J_p = 0.01, 0.1, 1.0$, only the ground state corresponds to the optimal solution. Since these properties are preserved in Ising machines, the periodic-boundary stacked model with antiferromagnetic interactions is effective for other ground-state search algorithms.

By contrast, in the open-boundary stacked model and the penalty spin model, the first- or second-excited states do not correspond to success states. As a result, adiabatic evolution is necessary to reach the ground state. In these QAC models, adding interactions enlarges the energy gap between the ground and first excited states, facilitating adiabatic evolution and improving performance.

Finally, note that in noisy or embedded settings, certain states may become stabilized due to hardware-specific effects. Under such conditions, models that inherently diversify sampled solutions, such as the periodic-boundary stacked model, exhibit superior performance. This observation is consistent with the high success probabilities observed experimentally on the quantum annealer.

V. CONCLUSION

We examined the properties of QAC models with additional interactions in QA characterized by a small energy gap, using the frustrated ring model as a benchmark. By employing the frustrated ring model, we ensured that the observed performance reflected intrinsic properties of QAC models rather than embedding artifacts. As a result, we demonstrated the potential of QAC models to

overcome limitations of conventional QA. Furthermore, this study provides insights into the mechanisms underlying the performance improvement.

Experiments on the actual quantum annealer and numerical simulations revealed that antiferromagnetic interactions enhance the success probability, whereas ferromagnetic interactions suppress it. Upon decoding, the QAC models yield various eigenstates corresponding to the optimal solution of the unprotected model. Notably, incorporating antiferromagnetic interactions within the QAC models significantly increases the success probability, even at short annealing times. This suggests that the QAC models are a promising strategy for hardware with limited coherence time and control noise.

We demonstrated that frustration introduced by periodic boundary conditions plays a key role in diversifying low-energy configurations, thereby enabling higher success probabilities even in the short annealing-time regime. These findings suggest that the QAC models can facilitate diabatic QA under limited annealing times.

In the future, our results suggest several promising directions. First, optimizing the interaction strength relative to the annealing time is essential to balance the benefits of replica frustration against the detrimental effects of large energy scales. Second, developing hardware-aware QAC models, tailored to specific connectivity and embedding constraints, will be vital for future QA platforms. Since constraints in combinatorial optimization are typically imposed as penalties, many problems reduce to dense Ising models. For practical applications, it is crucial to develop approaches that minimize embedding overhead and clarify how embedding affects performance. Finally, extending the present framework to more general optimization problems will further elucidate the role of frustration and interaction tuning in achieving scalability in quantum annealers.

ACKNOWLEDGMENTS

This work was partially supported by the Japan Society for the Promotion of Science (JSPS) KAKENHI (Grant Number JP23H05447), the Council for Science, Technology, and Innovation (CSTI) through the Cross-ministerial Strategic Innovation Promotion Program (SIP), “Promoting the application of advanced quantum technology platforms to social issues” (Funding agency: QST), Japan Science and Technology Agency (JST) (Grant Number JPMJPF2221). The computations in this work were partially performed using the facilities of the Supercomputer Center, the Institute for Solid State Physics, The University of Tokyo. S. Tanaka wishes to express their gratitude to the World Premier International Research Center Initiative (WPI), MEXT, Japan, for their support of the Human Biology-Microbiome-Quantum Research Center (Bio2Q). T. H. was supported by JST SPRING (Grant Number JPMJSP2123).

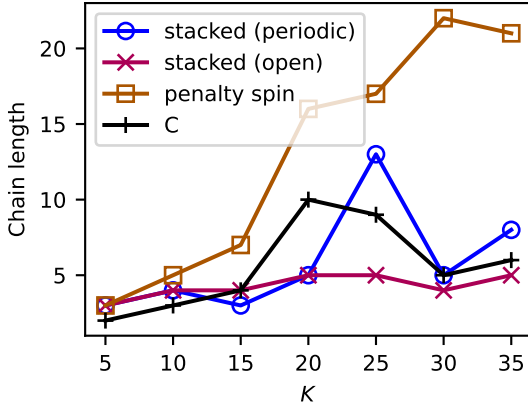


FIG. 10. The maximum chain length as a function of the number of replicas K for different QAC models. The problem size is $N = 61$. Solid lines between points are provided as a guide to the eye.

Appendix A: Effects of embedding

In this section, we examined the effects of constructing embedding chains in a quantum annealer. We performed the embeddings with minor embedding [72, 73]. Ideally, all spins within the chain should take the same value. However, due to noise, insufficient chain strength, or conflicting problem interactions, some chains may break, causing spins within the same chain to disagree.

Figure 10 shows the maximum chain length for each QAC model. In the stacked models, the maximum chain length is significantly different from that of the classical model. Under the present problem setting, the penalty spin model requires the longest chain length. This occurs because, as the number of replicas increases, the number of interactions involving the penalty spins also grows. Longer chains are more susceptible to chain breaks, and avoiding them requires setting the chain strength, the interactions between spins in a chain, to large values. However, large chain strengths constrain the overall energy scale of the problem, reducing the solution quality. In the penalty spin model, we also observed greater variability in chain lengths. The fractions of penalty spins effectively diminish their role, suggesting that the stacked model becomes more advantageous as the underlying problem becomes denser.

Figure 11 shows the chain-break fraction for each QAC model. Ideally, the spins in a chain are aligned in the same direction. The chain-break fraction is the ratio of the number of misaligned spins to the total number of spins in a chain. This metric serves as an indicator of embedding overhead and correlates with the susceptibility of chain breaks.

The results indicate that the chain-break fraction is significantly larger in the penalty spin model shown in Fig. 11 (c) than the open-boundary and periodic-boundary stacked models shown in Figs. 11 (a) and (b).

Our results demonstrate that the stacked model is more embedding-friendly. The reason is that, in the penalty spin model, the maximum number of interactions per spin grows as the sum of $(K - 1)$ along the parallelization directions and the number of interactions in the unprotected model. In the stacked model, by contrast, the contribution from parallelization is limited to two, regardless of K . Consequently, for $K \geq 3$, the interaction density is lower in the stacked model than in the penalty spin model.

These results suggest that certain QAC models are inherently better suited to the topology of specific hardware architectures, and that the development of QAC models tailored to future hardware topologies will be essential for minimizing embedding overhead.

Appendix B: Success probability in a short annealing time

In this section, we examined the size scaling and parameter dependence of the QAC models in a short annealing-time regime. Although the previous figures presented results for $\tau = 2000 \mu s$, here we focus on the case of $\tau = 1 \mu s$. Figure 12 shows the size dependence of the success probability at $\tau = 1 \mu s$.

For a short annealing time, the classical model ($J_p = 0.0$) exhibits a pronounced decrease in success probability as the problem size increases. By contrast, when negative J_p are introduced, the size dependence is significantly weakened, and the success probability becomes higher than that of the classical model. This demonstrates that antiferromagnetic interactions provide a clear advantage even in the short-time regime, consistent with the results obtained for long annealing times.

Moreover, the success probabilities achieved by the QAC models at $\tau = 1 \mu s$ are comparable to those of the classical model with annealing times in the range $\tau = 100\text{--}1000 \mu s$. This result highlights the effectiveness of QAC models in environments constrained by coherence times and noise. The results further indicate that leveraging a larger number of qubits can mitigate noise effects, suggesting that QAC models may serve as practical error-mitigation strategies for noisy quantum computers.

Figure 13 shows the success probability as a function of the strength of the additional interaction. The results confirm once again that parallelization with antiferromagnetic interactions yields higher success probabilities. However, in contrast to the previous results, we observe that for strong antiferromagnetic interactions ($J_p = -1$), the success probability is lower than for weaker interactions ($J_p = -0.1$). This indicates that in the short annealing-time regime, careful tuning of the interaction strength is required.

We attribute this to the stronger impact of the energy scale at short annealing times. As the annealing time decreases, the relative effect of large interaction strengths becomes increasingly pronounced. This finding also im-

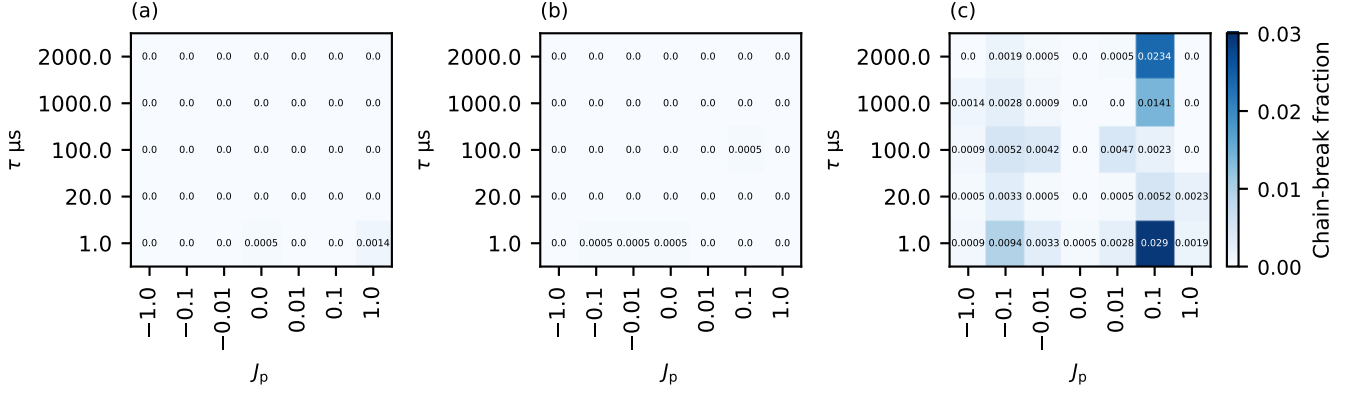


FIG. 11. The chain-break fractions as a function of the interaction strength J_p and the annealing time τ μ s for different QAC models. The problem size is $N = 61$, with the number of replicas fixed at $K = 35$. Panels show (a) periodic-boundary stacked model, (b) open-boundary stacked model, and (c) penalty spin model. The results at $J_p = 0$ correspond to the classical model with $K = 35$.

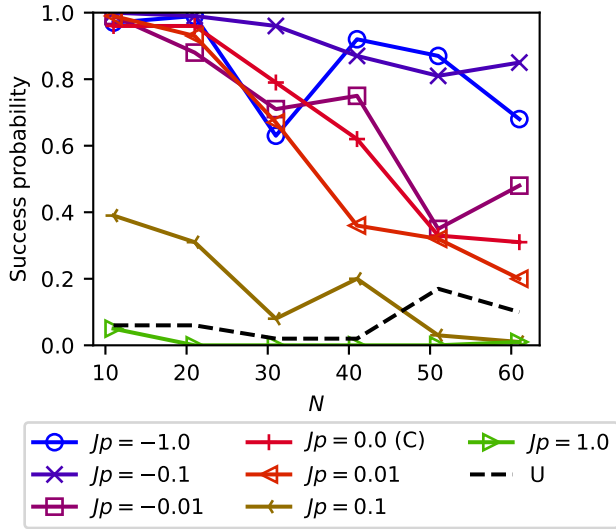


FIG. 12. Scaling of the final success probability of the periodic-boundary stacked model. The number of replicas is fixed to $K = 35$. The annealing time is $\tau = 1$ μ s. The results at $J_p = 0$ correspond to the classical model. The dashed black line represents the result of the success probability with the unprotected model. Solid lines between points are provided as a guide to the eye.

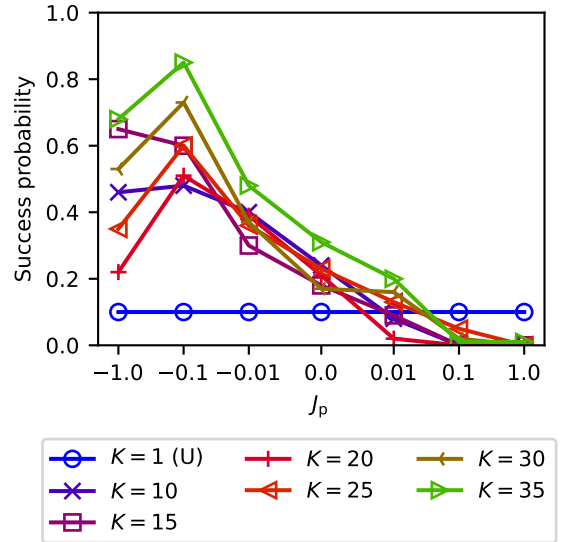


FIG. 13. The final success probability as a function of the interaction strength J_p with the periodic-boundary stacked model. The problem size is $N = 61$. The annealing time is $\tau = 1$ μ s. The results at $J_p = 0$ correspond to the classical model. A symmetric logarithmic scale is used for the horizontal axis to capture variations around zero. The results at $K = 1$ show the results of the unprotected model. Solid lines between points are provided as a guide to the eye.

Appendix C: Success probability in a frustrated ring model

plies that even in the periodic-boundary stacked model, where frustration enhances performance, the energy-scale effect can reduce the success probability. Furthermore, as the problem size and number of replicas increase, the number of interactions grows, making the energy-scale effect even more dominant.

In this section, we present the success probabilities of the QAC models applied to the frustrated ring model defined in Eq. (10). The energy gap of this model has been analytically studied in previous works, and it is known to close exponentially in the limit of infinite system size

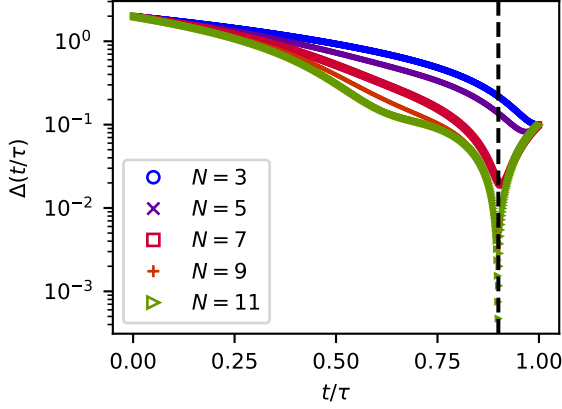


FIG. 14. Energy gap $\Delta(t/\tau)$ between the ground state and the first excited state during QA for the frustrated ring model. The interaction parameters are $J = 1$, $J_L = 0.45$ and $J_R = 0.5$. The black dashed line indicates the time at which the energy gap closes at $N \rightarrow \infty$, obtained analytically from the frustrated ring model defined in Eq. (10).

N . Figure 14 shows the energy gap of the frustrated ring model, obtained by exact diagonalization. As N increases, the energy gap closes, the ground state becomes degenerate between the all-up and all-down spin configurations, and the first excited state is fourfold degenerate.

Figure 15 shows the success probability as a function of J_p and τ . For the unprotected model, the success probability remains below 0.1 in most cases, regardless of the annealing time. The settings of the actual quantum annealer are the same as those in Section II. Consistent with the results in Section IV, high success probabilities are obtained with antiferromagnetic interactions. In particular, for the periodic-boundary stacked model, the success probability is enhanced over a broader parameter range than when degeneracy is lifted. This improvement is attributed to the fourfold degeneracy of the first excited state, which provides a diversity of accessible states and enables high success probabilities even at shorter annealing times. Thus, for degenerate problems, the diversity of solutions enhances the likelihood that the excited states of the parallelized model correspond to the correct solutions. This property confirms the effectiveness of QAC models even in degenerate systems.

The open-boundary stacked model also exhibits a wide parameter region with high success probabilities, indicat-

ing that QAC models are effective even without frustration. However, for large absolute values of the interaction strength, the success probability decreases, which we attribute to energy-scale effects. Therefore, the alleviation of fine-tuning requirements by frustration is consistent with our interpretation.

The penalty spin model exhibits qualitatively similar behavior. Adding interactions of small absolute magnitude increases the success probability, and when antiferromagnetic interactions are introduced, the success probability is particularly enhanced due to the decoding of the penalty spins.

Taken together, these results demonstrate that for problems otherwise hard to solve with quantum annealing, spatial parallelization combined with additional interactions provides a viable strategy. This highlights the potential of QAC models as near-term algorithms applicable to a wide range of problems.

Appendix D: Probability of the classical model

The classical model facilitates obtaining the optimal solution through decoding. In this section, we discuss the probabilities associated with the classical model. When the ground state is non-degenerate, the number n_{suc} of success states in the classical model with N spins and K replicas is given by

$$n_{\text{suc}} = \sum_{k=1}^K \binom{N}{K-k+1} (2^N - 1)^{k-1}. \quad (\text{D1})$$

Here, each replica is independent in the classical model.

If the success probability of the unprotected model is denoted by p_{success}^U , the success probability of the classical model is given by

$$p_{\text{success}}^C = 1 - (1 - p_{\text{success}}^U)^K. \quad (\text{D2})$$

The ground-state probability of the classical model is given by

$$p_{\text{gs}}^C = (p_{\text{gs}}^U)^K. \quad (\text{D3})$$

We confirmed that the probabilities of the classical model shown in Fig. 7 follow Eq. (D2).

-
- [1] T. Kadowaki and H. Nishimori, Quantum annealing in the transverse Ising model, *Phys. Rev. E* **58**, 5355 (1998).
 - [2] E. Farhi, J. Goldstone, S. Gutmann, and M. Sipser, Quantum computation by adiabatic evolution, arXiv preprint quant-ph/0001106 (2000).
 - [3] C. C. McGeoch, *Adiabatic quantum computation and quantum annealing: Theory and practice* (Morgan &

- Claypool Publishers, 2014).
- [4] S. Tanaka, R. Tamura, and B. K. Chakrabarti, *Quantum spin glasses, annealing and computation* (Cambridge University Press, 2017).
- [5] T. Albash and D. A. Lidar, Adiabatic quantum computation, *Rev. Mod. Phys.* **90**, 015002 (2018).
- [6] B. K. Chakrabarti, H. Leschke, P. Ray, T. Shirai, and

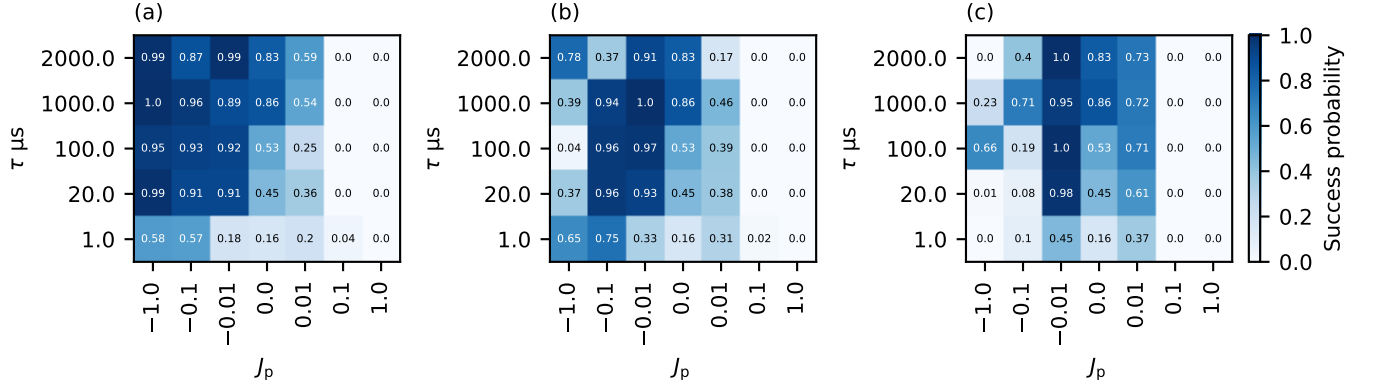


FIG. 15. Final success probability of QAC models on an actual quantum annealer as a function of the interaction strength J_p and the annealing time τ μ s. The blue bars represent the final success probability. The problem size is $N = 61$, with the number of replicas fixed at $K = 35$. Panels show (a) the periodic-boundary stacked model, (b) the open-boundary stacked model, and (c) the penalty spin model. The results at $J_p = 0$ correspond to the classical model with $K = 35$.

- S. Tanaka, Quantum annealing and computation: challenges and perspectives, *Philos. Trans. R. Soc. A* **381**, 20210419 (2023).
- [7] H. Karimi and G. Rosenberg, Boosting quantum annealer performance via sample persistence, *Quantum Inf. Process.* **16**, 166 (2017).
- [8] H. Karimi, G. Rosenberg, and H. G. Katzgraber, Effective optimization using sample persistence: A case study on quantum annealers and various Monte Carlo optimization methods, *Phys. Rev. E* **96**, 043312 (2017).
- [9] H. Irie, H. Liang, T. Doi, S. Gongyo, and T. Hatsuda, Hybrid quantum annealing via molecular dynamics, *Sci. Rep.* **11**, 8426 (2021).
- [10] Y. Atobe, M. Tawada, and N. Togawa, Hybrid annealing method based on subQUBO model extraction with multiple solution instances, *IEEE Trans. Comput.* **71**, 2606 (2022).
- [11] S. Kikuchi, N. Togawa, and S. Tanaka, Hybrid optimization method using simulated-annealing-based Ising machine and quantum annealer, *J. Phys. Soc. Jpn.* **92**, 124002 (2023), <https://doi.org/10.7566/JPSJ.92.124002>.
- [12] T. Hattori, H. Irie, T. Kadowaki, and S. Tanaka, Advantages of fixing spins in quantum annealing, *J. Phys. Soc. Jpn.* **94**, 013001 (2025).
- [13] T. Hattori, H. Irie, T. Kadowaki, and S. Tanaka, Impact of fixing spins in a quantum annealer with energy rescaling, *J. Phys. Soc. Jpn.* **94**, 074001 (2025).
- [14] S. Hiram and M. Ohzeki, Efficient algorithm for binary quadratic problem by column generation and quantum annealing, *J. Phys. Soc. Jpn.* **92**, 113002 (2023).
- [15] H. Kanai, M. Yamashita, K. Tanahashi, and S. Tanaka, Annealing-assisted column generation for inequality-constrained combinatorial optimization problems, *IEEE Access* **12**, 157669 (2024).
- [16] T. Hattori and S. Tanaka, Controlled diagonal catalyst improves the efficiency of quantum annealing, *arXiv preprint arXiv:2503.15244* (2025).
- [17] M. H. Amin, A. D. King, J. Raymond, R. Harris, W. Bernoudy, A. J. Berkley, K. Boothby, A. Smirnov, F. Altomare, M. Babcock, *et al.*, Quantum error mitigation in quantum annealing, *arXiv preprint arXiv:2311.01306* (2023).
- [18] Y. Shingu, T. Nikuni, S. Kawabata, and Y. Matsuzaki, Quantum annealing with error mitigation, *Phys. Rev. A* **109**, 042606 (2024).
- [19] K. Tanahashi, S. Takayanagi, T. Motohashi, and S. Tanaka, Application of Ising machines and a software development for Ising machines, *J. Phys. Soc. Jpn.* **88**, 061010 (2019).
- [20] K. Kitai, J. Guo, S. Ju, S. Tanaka, K. Tsuda, J. Shiomi, and R. Tamura, Designing metamaterials with quantum annealing and factorization machines, *Phys. Rev. Res.* **2**, 013319 (2020).
- [21] S. Izawa, K. Kitai, S. Tanaka, R. Tamura, and K. Tsuda, Continuous black-box optimization with an Ising machine and random subspace coding, *Phys. Rev. Res.* **4**, 023062 (2022).
- [22] T. Inoue, Y. Seki, S. Tanaka, N. Togawa, K. Ishizaki, and S. Noda, Towards optimization of photonic-crystal surface-emitting lasers via quantum annealing, *Opt. Express* **30**, 43503 (2022).
- [23] T. Matsumori, M. Taki, and T. Kadowaki, Application of QUBO solver using black-box optimization to structural design for resonance avoidance, *Sci. Rep.* **12**, 12143 (2022).
- [24] K. Nawa, T. Suzuki, K. Masuda, S. Tanaka, and Y. Miura, Quantum annealing optimization method for the design of barrier materials in magnetic tunnel junctions, *Phys. Rev. Appl.* **20**, 024044 (2023).
- [25] Y. Couzinié, Y. Seki, Y. Nishiyama, H. Nishi, T. Kosugi, S. Tanaka, and Y.-i. Matsushita, Machine learning supported annealing for prediction of grand canonical crystal structures, *J. Phys. Soc. Jpn.* **94**, 044802 (2025).
- [26] R. Tamura, Y. Seki, Y. Minamoto, K. Kitai, Y. Matsuda, S. Tanaka, and K. Tsuda, Black-box optimization using factorization and Ising machines, *arXiv preprint arXiv:2507.18003* (2025).
- [27] R. Harris, Y. Sato, A. J. Berkley, M. Reis, F. Altomare, M. Amin, K. Boothby, P. Bunyk, C. Deng, C. Enderud, *et al.*, Phase transitions in a programmable quantum spin glass simulator, *Science* **361**, 162 (2018).
- [28] A. D. King, J. Carrasquilla, J. Raymond, I. Ozfidan,

- E. Andriyash, A. Berkley, M. Reis, T. Lanting, R. Harris, F. Altomare, *et al.*, Observation of topological phenomena in a programmable lattice of 1,800 qubits, *Nature* **560**, 456 (2018).
- [29] K. Endo, Y. Matsuda, S. Tanaka, and M. Muramatsu, A phase-field model by an Ising machine and its application to the phase-separation structure of a diblock polymer, *Sci. Rep.* **12**, 10794 (2022).
- [30] R. Honda, K. Endo, T. Kaji, Y. Suzuki, Y. Matsuda, S. Tanaka, and M. Muramatsu, Development of optimization method for truss structure by quantum annealing, *Sci. Rep.* **14**, 13872 (2024).
- [31] Z. Xu, W. Shang, S. Kim, E. Lee, and T. Luo, Quantum annealing-assisted lattice optimization, *npj Comput. Mater.* **11**, 4 (2025).
- [32] G. Rosenberg, P. Haghnegahdar, P. Goddard, P. Carr, K. Wu, and M. L. De Prado, Solving the optimal trading trajectory problem using a quantum annealer, in *Proceedings of the 8th workshop on high performance computational finance* (2015) pp. 1–7.
- [33] E. Grant, T. S. Humble, and B. Stump, Benchmarking quantum annealing controls with portfolio optimization, *Phys. Rev. Appl.* **15**, 014012 (2021).
- [34] T. Kato, On the adiabatic theorem of quantum mechanics, *J. Phys. Soc. Jan.* **5**, 435 (1950).
- [35] A. Lucas, Ising formulations of many NP problems, *Front. Phys.* **2**, 5 (2014).
- [36] B. Altshuler, H. Krovi, and J. Roland, Anderson localization makes adiabatic quantum optimization fail, *Proceedings of the National Academy of Sciences* **107**, 12446 (2010).
- [37] A. Pearson, A. Mishra, I. Hen, and D. A. Lidar, Analog errors in quantum annealing: doom and hope, *npj Quantum Inf.* **5**, 107 (2019).
- [38] T. Albash and D. A. Lidar, Decoherence in adiabatic quantum computation, *Phys. Rev. A* **91**, 062320 (2015).
- [39] Y. Seki and H. Nishimori, Quantum annealing with antiferromagnetic fluctuations, *Phys. Rev. E* **85**, 051112 (2012).
- [40] R. D. Somma, D. Nagaj, and M. Kieferová, Quantum speedup by quantum annealing, *Phys. Rev. Lett.* **109**, 050501 (2012).
- [41] Y. Susa, Y. Yamashiro, M. Yamamoto, and H. Nishimori, Exponential speedup of quantum annealing by inhomogeneous driving of the transverse field, *J. Phys. Soc. Jpn.* **87**, 023002 (2018).
- [42] Y. Susa, Y. Yamashiro, M. Yamamoto, I. Hen, D. A. Lidar, and H. Nishimori, Quantum annealing of the p-spin model under inhomogeneous transverse field driving, *Phys. Rev. A* **98**, 042326 (2018).
- [43] J. I. Adame and P. L. McMahon, Inhomogeneous driving in quantum annealers can result in orders-of-magnitude improvements in performance, *Quantum Sci. Technol.* **5**, 035011 (2020).
- [44] T. Albash and M. Kowalsky, Diagonal catalysts in quantum adiabatic optimization, *Phys. Rev. A* **103**, 022608 (2021).
- [45] T. Zaborniak and R. Sousa, Benchmarking Hamiltonian Noise in the D-Wave Quantum Annealer, *IEEE Trans. Quantum Eng.* **2**, 3100206 (2021).
- [46] N. Feinstein, L. Fry-Bouriaux, S. Bose, and P. A. Warburton, Effects of XX catalysts on quantum annealing spectra with perturbative crossings, *Phys. Rev. A* **110**, 042609 (2024).
- [47] R. Ghosh, L. A. Nutricati, N. Feinstein, P. A. Warburton, and S. Bose, Exponential speed-up of quantum annealing via n-local catalysts, *arXiv preprint arXiv:2409.13029* (2024).
- [48] E. Crosson and D. Lidar, Prospects for quantum enhancement with diabatic quantum annealing, *Nat. Rev. Phys.* **3**, 466 (2021).
- [49] J. Côté, F. Sauvage, M. Larocca, M. Jonsson, L. Cincio, and T. Albash, Diabatic quantum annealing for the frustrated ring model, *Quantum Sci. and Technol.* **8**, 045033 (2023).
- [50] N. Feinstein, I. Shalashilin, S. Bose, and P. Warburton, Robustness of diabatic enhancement in quantum annealing, *Quantum Sci. Technol.* **10**, 025011 (2025).
- [51] E. Pelofske, G. Hahn, and H. N. Djidjev, Parallel quantum annealing, *Sci. Rep.* **12**, 4499 (2022).
- [52] K. L. Pudenz, T. Albash, and D. A. Lidar, Error-corrected quantum annealing with hundreds of qubits, *Nat. Commun.* **5**, 3243 (2014).
- [53] K. L. Pudenz, T. Albash, and D. A. Lidar, Quantum annealing correction for random Ising problems, *Phys. Rev. A* **91**, 042302 (2015).
- [54] W. Vinci, T. Albash, G. Paz-Silva, I. Hen, and D. A. Lidar, Quantum annealing correction with minor embedding, *Phys. Rev. A* **92**, 042310 (2015).
- [55] W. Vinci, T. Albash, G. Paz-Silva, I. Hen, and D. A. Lidar, Quantum annealing correction with minor embedding, *Phys. Rev. A* **92**, 042310 (2015).
- [56] W. Vinci, T. Albash, and D. A. Lidar, Nested quantum annealing correction, *npj Quantum Inf.* **2**, 1 (2016).
- [57] S. Matsuura, H. Nishimori, T. Albash, and D. A. Lidar, Mean field analysis of quantum annealing correction, *Phys. Rev. Lett.* **116**, 220501 (2016).
- [58] A. Mishra, T. Albash, and D. A. Lidar, Performance of two different quantum annealing correction codes, *Quantum Inf. Process.* **15**, 609 (2016).
- [59] S. Matsuura, H. Nishimori, W. Vinci, T. Albash, and D. A. Lidar, Quantum-annealing correction at finite temperature: Ferromagnetic p-spin models, *Phys. Rev. A* **95**, 022308 (2017).
- [60] W. Vinci and D. A. Lidar, Scalable effective-temperature reduction for quantum annealers via nested quantum annealing correction, *Phys. Rev. A* **97**, 022308 (2018).
- [61] S. Matsuura, H. Nishimori, W. Vinci, and D. A. Lidar, Nested quantum annealing correction at finite temperature: p-spin models, *Phys. Rev. A* **99**, 062307 (2019).
- [62] J. Bennett, A. Callison, T. O’Leary, M. West, N. Chancellor, and V. Kendon, Using copies can improve precision in continuous-time quantum computing, *Quantum Sci. Technol.* **8**, 035031 (2023).
- [63] K. Hino and S. Tanaka, Physical properties of error reduction algorithms for Ising machines, in *2024 IEEE International Conference on Quantum Computing and Engineering (QCE)*, Vol. 02 (2024) pp. 434–435.
- [64] R. Y. Li, T. Albash, and D. A. Lidar, Improved Boltzmann machines with error corrected quantum annealing, *arXiv preprint arXiv:1910.01283* (2019).
- [65] R. Y. Li, T. Albash, and D. A. Lidar, Limitations of error corrected quantum annealing in improving the performance of Boltzmann machines, *Quantum Sci. Technol.* **5**, 045010 (2020).
- [66] K. C. Young, R. Blume-Kohout, and D. A. Lidar, Adiabatic quantum optimization with the wrong hamiltonian, *Phys. Rev. A* **88**, 062314 (2013).

- [67] D. Roberts, L. Cincio, A. Saxena, A. Petukhov, and S. Knysh, Noise amplification at spin-glass bottlenecks of quantum annealing: A solvable model, *Phys. Rev. A* **101**, 042317 (2020).
- [68] R. Wang, V. R. Arezzo, K. Thengil, G. Pecci, and G. E. Santoro, From exponential to quadratic: Optimal control for a frustrated Ising ring model, *Quantum Sci. Technol.* (2025).
- [69] S. Kirkpatrick, C. D. Gelatt Jr, and M. P. Vecchi, Optimization by simulated annealing, *Science* **220**, 671 (1983).
- [70] Per-QPU solver properties and schedules, https://docs.dwavequantum.com/en/latest/quantum_research/solver_properties_specific.html#advantage2-system1-6, (accessed 2025-9-11).
- [71] A. Boothby, K. and King and J. Raymond, Zephyr topology of D-Wave quantum processors (2021).
- [72] V. Choi, Minor-embedding in adiabatic quantum computation: I. The parameter setting problem, *Quantum Inf. Process.* **7**, 193 (2008).
- [73] V. Choi, Minor-embedding in adiabatic quantum computation: II. Minor-universal graph design, *Quantum Inf. Process.* **10**, 343 (2011).
- [74] J. Johansson, P. D. Nation, and F. Nori, QuTiP: An open-source Python framework for the dynamics of open quantum systems., *Phys. Comm.* **183**, 1760 (2012).
- [75] J. Johansson, P. D. Nation, and F. Nori, QuTiP 2: A Python framework for the dynamics of open quantum systems., *Phys. Comm.* **184**, 1234 (2013).